PAPER

Check for updates

Ultra-high energy density supercapacitors using a nickel phosphide/nickel/titanium carbide nanocomposite capacitor electrode†

Jing Xu,[a] Nianjun Yang, [ID] *[a] Siyu Yu,[a,b] Anna Schulte,[c] Holger Schönherr [ID] [c] and Xin Jiang*[a]

The low energy density of traditional supercapacitors has strongly restricted their applications. The utilization of novel capacitor electrodes to enhance the energy densities of supercapacitors is thus of great significance. Herein, a binder-free $Ni_{12}P_5$/Ni/TiC nanocomposite film is synthesized and further employed as the capacitor electrode. This nanocomposite film is grown by means of a chemical vapor deposition process, where Ni_5TiO_7 nanowires and a TiO_2 layer are *in situ* converted into hierarchical interconnected three-dimensional (3D) $Ni/Ni_{12}P_5$ nanoparticles and a porous TiC matrix, respectively. Such a nanocomposite film exhibits an extremely high specific surface area and excellent conductivity, leading to its high capacitive performance. Remarkably, the multiple redox states of Ni species, namely two pairs of redox waves are observed in neutral aqueous solutions. At a current density of 10 mA cm^{-2}, its specific capacitance in 1 M Na_2SO_4 aqueous solution is as high as 160.0 mF cm^{-2}. The maximal energy density of a supercapacitor fabricated with this nanocomposite capacitor electrode is 42.6 W h kg^{-1} at a power density of 1550 W kg^{-1}. Such an ultra-high energy density is even comparable with that of Li-batteries. The proposed supercapacitor thus has high potential for industrial applications.

Introduction

Driven by the shortage of fossil resources and rapidly growing demands on energy consumption, tremendous efforts have been made to explore and develop suitable energy storage and conversion strategies, technologies, and devices. Among various electrochemical energy storage devices, supercapacitors (SCs) are considered as an exclusive class.[1] According to the charge storage mechanisms, SCs can be classified into electrical double layer capacitors (EDLCs) and pseudocapacitors (PCs). EDLCs are based on ion adsorption/desorption at the surface of capacitor electrodes, while PCs rely on surface-controlled faradaic reactions of redox-active species coated on the electrode. SCs feature desirable properties, such as high power densities, excellent cycling stabi-

lity, and fast charging/discharging rates. Therefore, they can complement or even replace Li-batteries in some particular applications. Unfortunately, conventional SCs provide insufficient energy densities (2–5 W h kg^{-1}) when compared with batteries.[2–5] On the other hand, PCs are expected to exhibit enhanced SC performance (namely high capacitances and enhanced energy densities) since the PC capacitor electrodes involve fast and reversible redox reactions.[6] To further enhance the SC performance, a PC electrode featuring a high and accessible surface area, excellent conductivity, and outstanding stability is more favorable.

To date, various PC capacitor electrodes have been synthesized and applied for the construction of high-performance SCs.[1–6] Among them, Ni-based materials are one of the extensively reported PC capacitor electrodes. This is due to their abundance and easy availability. For example, nickel oxide/hydroxide ($NiO/Ni(OH)_2$) PC capacitor electrodes have been frequently utilized. Unfortunately, their low electric conductivities led to relative low power densities of these PCs. Due to the excellent electric conductivities and superior redox activities of nickel phosphides (*e.g.*, NiP_2, $Ni_{12}P_5$, Ni_2P, *etc.*), they have been proposed to replace these oxide/hydroxide PC capacitor electrodes.[7,8] For example, a specific capacitance of 2141 F g^{-1} has been obtained for a Ni_2P/Ni capacitor electrode, which is about three times higher than that of a $Ni(OH)_2$/Ni

[a]Institute of Materials Engineering, University of Siegen, 57076 Siegen, Germany.
E-mail: nianjun.yang@uni-siegen.de, xin.jiang@uni-siegen.de
[b]School of Chemistry and Chemical Engineering, Southwest University, Chongqing 400715, China
[c]Physical Chemistry I & Research Center of Micro and Nanochemistry and Engineering (Cμ), Department of Chemistry and Biology, University of Siegen, 57076 Siegen, Germany
†Electronic supplementary information (ESI) available. See DOI: 10.1039/d0nr01984d

capacitor electrode under identified conditions.[9] Among nano-capsule $Ni_{12}P_5$, flower-like NiO, and flower-like $Ni(OH)_2$ PC capacitor electrodes, the $Ni_{12}P_5$ nanocapsules exhibit the highest capacitance of 949 F g^{-1} at a current density of 1 A g^{-1}.[10] Although various methods (e.g., such as ball-milling[11] and hydrothermal process[12]) have been utilized to synthesize nickel phosphides, the as-produced nickel phosphides by these methods contain a lot of byproducts. In other words, the purities of nickel phosphides synthesized by these methods are low.[13,14] Moreover, they are only in the form of powders. A binder(s) and current collector are thus required for the construction of these nickel phosphide based PC capacitor electrodes. The novel approach to synthesize binder-free nickel phosphide based PC capacitor electrodes is thus highly demanded.

Herein, a binder-free $Ni_{12}P_5$/Ni/TiC nanocomposite film is synthesized by means of in situ carbonization/reduction of the precursors of Ni_5TiO_7 nanowires in a chemical vapor deposition (CVD) reactor. The P dopant is introduced into a porous TiO_2 layer in the course of a plasma electrolytic oxidation (PEO) process.[15] On this hierarchical film, $Ni/Ni_{12}P_5$ nanoparticles are coated on the top of a TiC layer. A three-dimensional (3D) network structure of this nanocomposite film leads to an extremely high specific surface, good permeability, and full exposure of active sites. Moreover, the TiC layer is porous and has excellent electric conductivity. In other words, it can serve as the current collector. Consequently, this novel $Ni_{12}P_5$/Ni/TiC/Ti nanocomposite film possesses all advantages of a capacitor electrode that are required for the construction of high-performance PCs. In this contribution, the investigation of the capacitive performance of this nanocomposite film (e.g., its capacitance, capacitance retention) in 1 M Na_2SO_4 solution and the evaluation on power densities and energy densities of the SCs constructed using this nanocomposite PC capacitor electrode are presented.

Results and discussion

Characterization of $Ni_{12}P_5$/Ni/TiC nanocomposite capacitor electrodes

X-ray diffraction is firstly applied to identity the crystalline structures of the as-synthesized films obtained after annealing and subsequent CVD treatment. The XRD patterns of the Ni_5TiO_7/TiO_2 nanocomposite film (a) and the one after its subsequent treatment with a described CVD process (b) are shown Fig. 1. The rutile TiO_2 (PDF#21-1276) and Ni_5TiO_7 phases (PDF#31-0917) are confirmed to be the two main phases before the CVD treatment, in good agreement with previous report.[16] After the CVD treatment, two groups of new diffraction peaks appear at 44.5°, 51.8°, and 73.4° and at 48.9°, 46.6°, and 38.4°, respectively. They are attributed to the metal Ni (PDF#70-1849) and $Ni_{12}P_5$ (PDF#74-1381), respectively. Note that, the Ni_5TiO_7 phase can be stoichiometrically considered as $5NiO·TiO_2$. The appearance of Ni thus results from the reduction of NiO by H_2 and CH_4 gases during the CVD process at high temperatures. The obvious and predominate peaks of
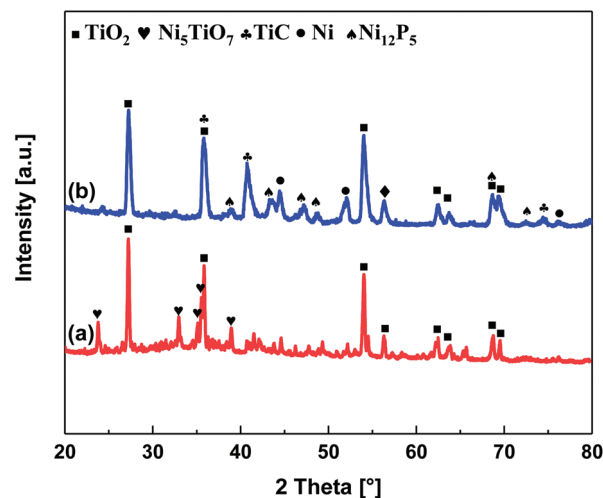

Fig. 1 XRD spectra of a Ni_5TiO_7/TiO_2 nanocomposite film before (a) and after (b) the CVD treatment for 15 min.

41.7° and 35.9° are attributed to cubic TiC crystals, implying the occurrence of a carbonization process. It is probably related to the reaction of TiO_2 with CH_4 during the CVD process.[19] It has to be pointed out that the rutile phase of TiO_2 does not completely disappear. This is because the porous TiO_2 layer formed by a PEO process is extremely thick. As proved by the cross-section SEM image of the Ni_5TiO_7/TiO_2 nanocomposite film (Fig. S1a†), its thickness (beneath the Ni_5TiO_7 nanowires) is about 6.0 μm. Consequently, the TiC layer is formed only at the top of the TiO_2 layer.

The SEM images and related EDX profiles of the as-prepared nanocomposite films before and after the CVD process are shown in Fig. 2. Straight and dense Ni_5TiO_7 nanowires are seen on the Ni_5TiO_7/TiO_2(P) nanocomposite film before the CVD process (Fig. 2a). The average diameter of these nanowires is about 190 nm and their surface is smooth (Fig. S1b†). The EDX line profile reveals that the overall surface consists mainly of the elements of Ti, Ni, O, and P (Fig. 2b). The element of P is from the used PEO electrolyte. It is believed that the electrolyte components can be dissociated to active ion- or atom-species due to the high energy discharges during the PEO.[17,18] This is confirmed by the EDX analysis of the PEO sample before the growth of the Ni_5TiO_7 nanowires (Fig. S2a†). Hence, the phosphorus ions are incorporated into the porous TiO_2 surface/matrix during the growth of the TiO_2 layer. Such phenomena are similar to those reported previously.[19,20] After the CVD treatment, the morphology of these Ni_5TiO_7 nanowires is greatly changed (Fig. 2c). Their surface is not smooth anymore. The surface of these nanowires appears to be coated with different particles, the sizes of which vary from 89 to 221 nm. These fibrous nanoparticles are actually aggregated with each other or further interconnected, leading to the formation of a 3D network structure. The EDX line profile of a local nanoparticle (Fig. 2d) reveals that these nanoparticles are mainly composed of the elements of Ni, P and C as well as a tiny amount of the elements of Ti and O. The existence of C
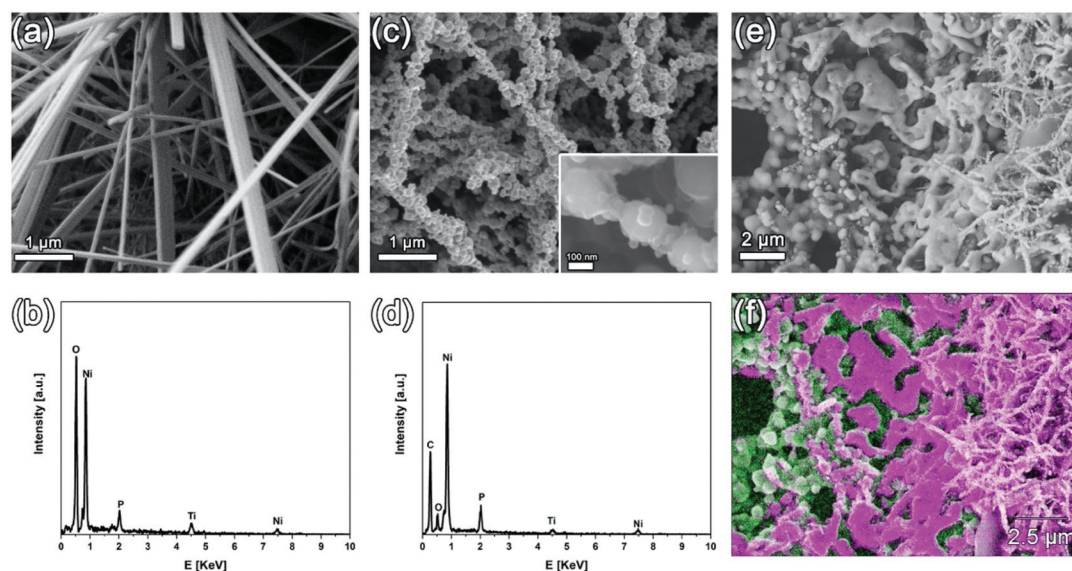
Fig. 2 (a) SEM image of the Ni_5TiO_7/TiO_2 nanocomposite film before the CVD treatment and (b) the EDX spectrum recorded from its overall surface; (c) SEM image of the superficial layer of an as-prepared $Ni_{12}P_5/Ni/TiC$ nanocomposite film and (d) related EDX spectrum recorded from a local nanoparticle; (e) SEM image of the partially exposed underlayer of the as-prepared $Ni_{12}P_5/Ni/TiC$ nanocomposite film after ultrasonic removal of the superficial layer and (f) the corresponding EDX mapping with the elements of Ti (green) and Ni (pink). The inset in (c) shows the SEM image of the $Ni_{12}P_5/Ni/TiC$ nanocomposite film (c) at a higher magnification.

element on the local nanoparticle suggests the formation of amorphous carbon. Further analysis of EDX line profiles on different nanoparticles reveals that the average atomic ratio of Ni to O is approximately 21 : 5, higher than the stoichiometry of $Ni_{12}P_5$. This indicates an excess amount of Ni element in this composite film, probably due to the existence of pure Ni atoms, as already observed from the XRD analysis of these nanoparticles. Note here that, it is believed that the variation of the atomic ratios of these elements (*e.g.*, Ni, P, and O) inside these nanoparticles actually affects their properties (*e.g.*, the capacitive performance of the as-fabricated $Ni_{12}P_5/Ni/TiC$ composite capacitor electrode). For a more precise calculation of the atomic ratios of these elements (*e.g.*, Ni, P, and O) in different nanoparticles and their structure (*e.g.*, a core–shell structure), the high-resolution transmission electron images of these nanoparticles are required.

To further investigate the structure of this nanocomposite film, it was treated in an ultrasonic bath for a few seconds. In this way, superficial nanoparticles were partially removed. The SEM image of a treated sample and its corresponding EDX mapping are shown in Fig. 2e and f, respectively. Two distinct structures are observed beneath the nanoparticle network: a porous bottom layer and a "melt-like" interlayer. The diameter of the pores in the bottom layer ranges from 0.7 to 2.8 μm. Such a porous layer is derived from the porous coating that is formed after the PEO treatment (Fig. S2b†). The formation of these pores is due to the discharging behavior during the PEO process.[21] The bottom of this porous layer is a Ti-rich area (Fig. 2f), indicating that this TiC layer is originally transformed from the as-formed TiO_2 layer during the PEO process. Moreover, a "melt-like" layer is covered on the top of pores.

Such an interlayer is actually a Ni-rich area. This "melt-like" layer is assumed to be formed *via* the reduction of NiO, which is derived from the thermal decomposition of $Ni(NO_3)_2$ during the annealing process.[22]

To further analyze the composition and the chemical bonding states of the Ni_5TiO_7/TiO_2 nanocomposite film after the CVD treatment, its XPS spectra were recorded. Its XPS survey spectrum (Fig. 3) confirms that the dominant element of the CVD treated Ni_5TiO_7/TiO_2 nanocomposite film is carbon (79.9%), suggesting the successful carbonization of Ni_5TiO_7 during the CVD process. Its high-resolution XPS spectra were then utilized to investigate the bonding state of Ti, C, Ni and P elements. For example, in its Ti 2p spectrum (Fig. 3a), two peaks are centered at 460.9 and 454.9 eV, which can be assigned to the Ti $2p_{1/2}$ and Ti $2p_{3/2}$ of the Ti^{4+} species, respectively.[23] The shoulder between them (at around 457.8 eV) indicates the existence of Ti in a lower valence. In its C 1s spectrum (Fig. 3b), the peak at 281.9 eV is attributed to metal–C binding, confirming again the formation of TiC. The rest of the peaks located at the binding energies of 284.4, 286.2, and 288.6 eV correspond to carbon in C–C (sp^2), C–O, and C=O, respectively. The sp^2 carbon indicates the existence of amorphous carbon in the composite film. In its Ni 2p spectrum (Fig. 3c), there are two dominating peaks centered at binding energies of 852.8 and 870.0 eV, ascribed to Ni $2p_{3/2}$ of metallic Ni^0.[24] Another two broad peaks at 855.1 and 873.5 eV can be assigned to Ni^{II}. Two additional peaks at 859.8 and 876.5 eV are assigned to the shake-up satellite structure of Ni $2p_{1/2}$. In its P 2p spectrum (Fig. 3d), the binding energy at 129.8 eV can be ascribed to phosphide (Ni–P). The peak appearing at 133.3 eV can be attributed to phosphate species, which may have
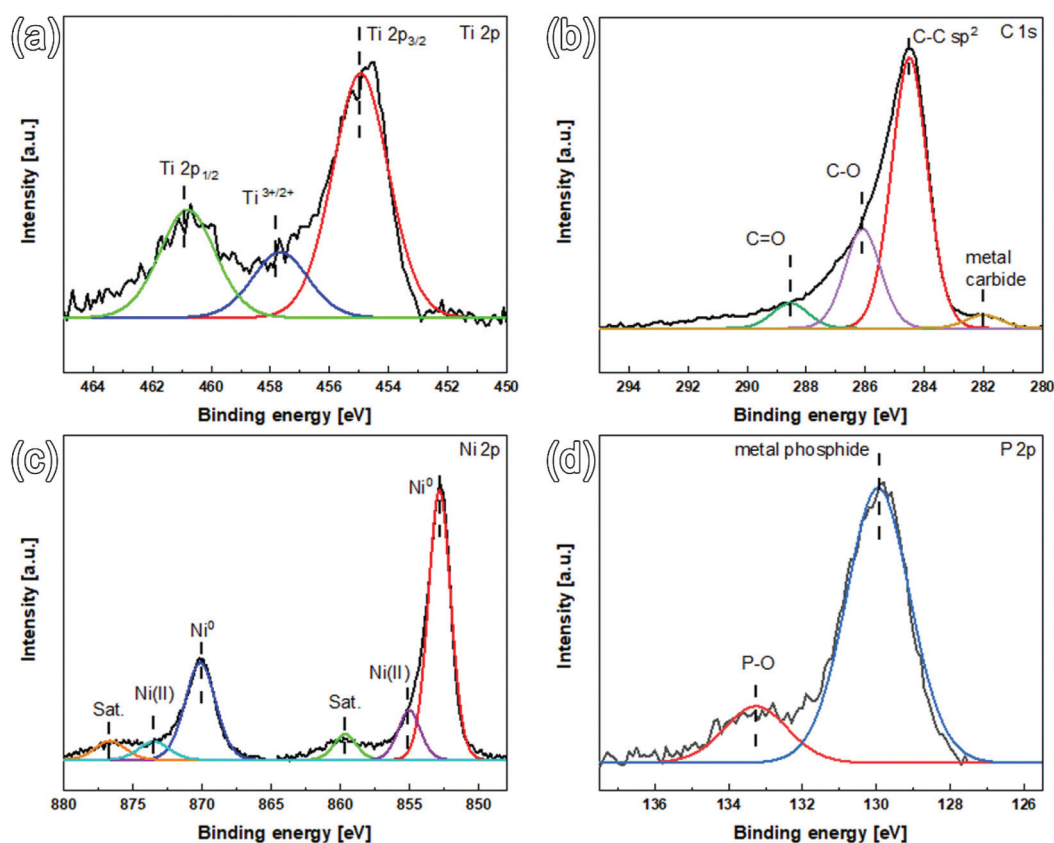
Fig. 3 High-resolution XPS spectra of (a) Ti 2p, (b) C 1s, (c) Ni 2p, and (d) P 2p core levels for the $Ni_{12}P_5$/Ni/TiC nanocomposite film.

been formed due to the exposure of the sample to air.[10,25] Therefore, in $Ni_{12}P_5$ the Ni species exhibits a slight positive charge (Ni^{x+}, $0 < x < 2$), while the P species has a small negative charge. Consequently, such a nanocomposite film features pseudocapacitive behavior.[7,8,10] Once it is utilized as capacitor electrodes, a high performance SC is expected to be constructed.

Pseudocapacitive performance of the $Ni_{12}P_5$/Ni/TiC nanocomposite capacitor electrode

The specific capacitances of the $Ni_{12}P_5$/Ni/TiC nanocomposite capacitor electrode were then evaluated in 1.0 M Na_2SO_4 aqueous solution by means of cyclic voltammetry and the galvanostatic charging/discharging method. Fig. 4a shows its cyclic voltammograms at different scan rates. A pair of pronounced redox waves are seen at all scan rates. The cathode and anodic peak potentials are located at about −0.09 and 0.1 V, respectively. Two reactions are assumed to be responsible for the behavior shown in Fig. 4a:[8,26]

$$Ni^{2+} + 2OH^- \leftrightarrow Ni(OH)_2 \tag{1}$$

$$Ni(OH)_2 + OH^- \leftrightarrow NiOOH + H_2O + e^- \tag{2}$$
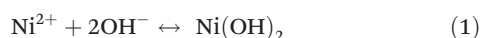
An increase of the scan rates leads to the linear enhancement of peak currents and enlarged peak difference (namely a positive shift of anodic peak potentials and meanwhile a nega-

tive shift of cathodic peak potentials). The redox process of this $Ni_{12}P_5$/Ni/TiC nanocomposite capacitor electrode is thus quasi-reversible. Notice that, these CVs are distinct from those for EDLCs, which are close to the ideal rectangular shape. Therefore, the $Ni_{12}P_5$/Ni/TiC nanocomposite capacitor electrode exhibits pseudocapacitive behavior. The calculated pseudocapacitances are 133.9, 92.5, 56.2, and 34.7 mF cm^{-2} at a scan rate of 10, 20, 50, and 100 mV s^{-1}, respectively.

Fig. 4b presents the galvanostatic charging/discharging (GCD) curves of the $Ni_{12}P_5$/Ni/TiC nanocomposite capacitor electrode at the current densities ranging from 10 to 30 mA cm^{-2}. The curves are non-linear but with equivalent charging and discharging times. Take the current density of 10 mA cm^{-2} as an example, the discharging time is *ca.* 21 s and the charging time is 29 s. This confirms the good reversibility of this PC electrode during the charging/discharging processes. Two voltage plateaus (from −0.1 to −0.07 V in the charging region, and from 0.08 to 0.11 V in the discharging domain) indicate that the redox reactions are dominated in the charging/discharging processes, in good agreement with the CV measurements. The estimated capacitances are 160.0, 84.3, 43.0, and 4.9 mF cm^{-2} at a current density of 10, 15, 20 and 30 mA cm^{-2}, respectively. The ultra-high specific capacitance of this $Ni_{12}P_5$/Ni/TiC nanocomposite capacitor electrode is believed to mainly originate from its unique nano-structural feature or its high surface area. In other words, the extremely
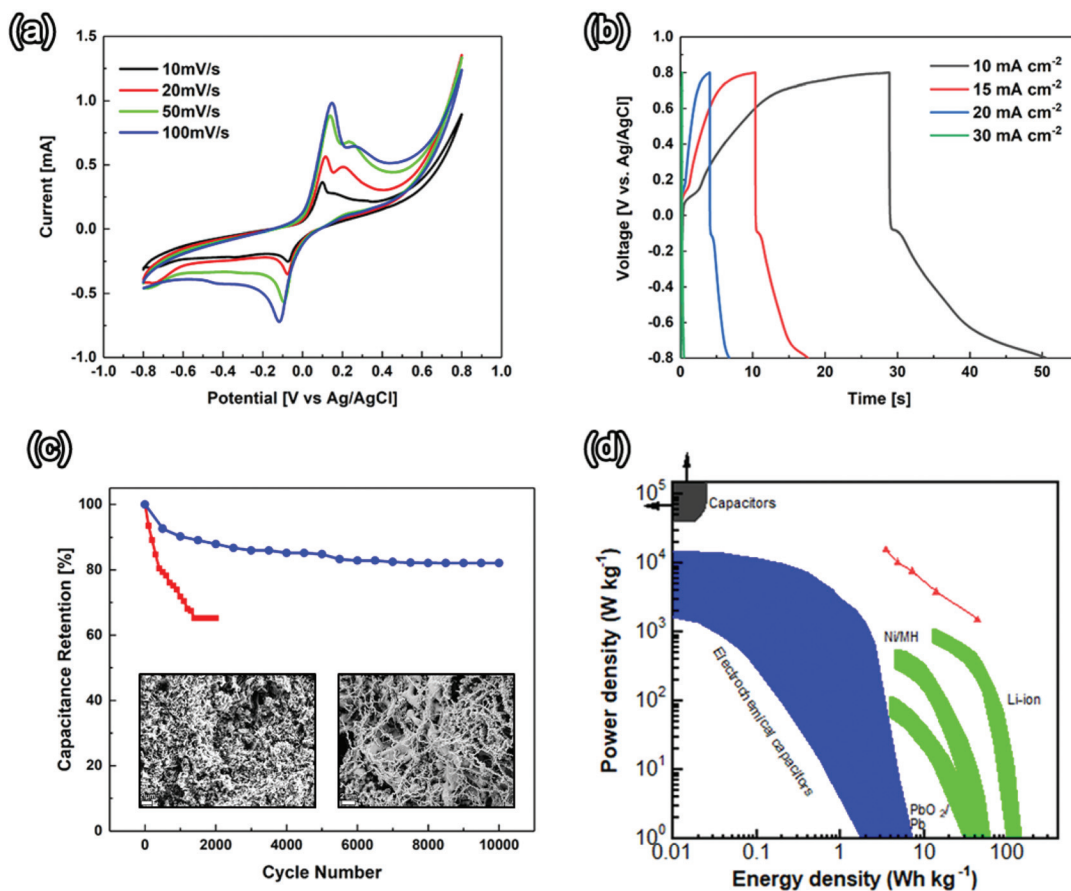
Fig. 4 (a) CVs and (b) GCD curves of a $Ni_{12}P_5/Ni/TiC$ nanocomposite capacitor electrode in 1.0 M Na_2SO_4 aqueous solution at different scan rates and current densities; (c) capacitance retention as a function of cycling numbers where the applied current density is 20 mA cm^{-2}. The insets in (c) are the SEM images of the $Ni_{12}P_5/Ni/TiC$ nanocomposite film after (left) 2000 and (right) 10 000 charging/discharging cycles. In the latter case, a $Ni_{12}P_5/Ni/TiC$ nanocomposite capacitor electrode was coated with a Nafion film. (d) Comparison of the Ragone plot of the PCs constructed using the $Ni_{12}P_5/Ni/TiC$ nanocomposite capacitor electrodes (orange line) in 1.0 M Na_2SO_4 aqueous solution with those of traditional capacitors, other electrochemical capacitors, different batteries, *etc*. Adapted with permission from ref. 28. Copyright 2008, Nature Publisher.

high specific surface of the $Ni_{12}P_5/Ni$ nanoparticles provides a large and pseudocapacitive surface area. Meanwhile, its hierarchical 3D network benefits accessibility to the electrolytes in solutions.

The long-term stability of the $Ni_{12}P_5/Ni/TiC$ nanocomposite capacitor electrode was tested by means of the GCD technique at a current density of 20 mA cm^{-2}. The capacitance retention is shown in Fig. 4c as a function of the cycling number. After the first 2000 cycles, the capacitance is reduced to 65% of its initial capacitance. To figure out possible reasons for this rapid reduction of the as-obtained capacitance, the $Ni_{12}P_5/Ni/TiC$ composite capacitor electrode was then examined using SEM after the cycling test. Surprisingly, its 3D network (shown in Fig. 2c) is partially destroyed (the left inset in Fig. 4c). Namely, some nanostructural features disappear, probably originating from surface damage during such a surface-controlled redox process and/or quasi-/ir-reversible surface re-construction in the course of the charging/discharging process. To avoid the rapid reduction of the as-obtained capacitances, the $Ni_{12}P_5/Ni/TiC$ nanocomposite capacitor electrode was then

coated with a thin Nafion membrane. Under this condition, the capacitance of the $Ni_{12}P_5/Ni/TiC$ nanocomposite capacitor electrode is only reduced to 82.1% of its initial value, even after 10 000 charging/discharging cycles. As expected, the surface morphology of the $Ni_{12}P_5/Ni/TiC$ composite capacitor electrode (the right inset in Fig. 4c) is nearly unchanged after such a long-term stability test.

A symmetrical two-electrode system was then constructed using $Ni_{12}P_5/Ni/TiC$ nanocomposite capacitor electrodes. It was further applied to calculate the energy (E) and power (P) densities of this PC device. The mass of active electrode materials was estimated by weighing the active films peeled from the Ti substrate. Fig. 4d shows a comparison of the gravimetric Ragone plot of this PC (namely P *vs*. E) with that of other capacitors and batteries. For example, the maximal E is 42.6 W h kg^{-1}, which is obtained at a P of 1550 W kg^{-1}. This energy density is even close to that of lithium batteries. Compared to some other reported phosphide based supercapacitors,[14,27] our device exhibits not only much higher E, but also higher P. For example, its energy density remains as
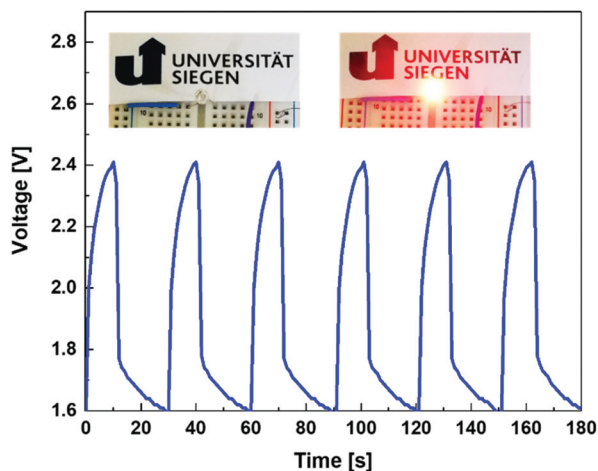
Fig. 5 Voltage-time curve during the charging/discharging of the PC demonstrator constructed using two $Ni_{12}P_5/Ni/TiC$ nanocomposite capacitor electrodes. The insets are the photos of the red LED status during charging (left) and discharging (right) processes.

3.5 W h kg^{-1} even at a power density of 15 762 W kg^{-1}. Such an excellent SC or PC performance is due to high pseudocapacitive behavior (or redox activity) of the $Ni_{12}P_5/Ni$ species in the $Ni_{12}P_5/Ni/TiC$ nanocomposite film. In addition, the excellent conductivities of $Ni_{12}P_5$, Ni, and TiC accelerate the exchange of the electrons between the electrode and the electrolytes, eventually bringing in improved pseudocapacitive behavior or SC performance of the $Ni_{12}P_5/Ni/TiC$ nanocomposite capacitor electrode.

A supercapacitor demonstrator was further constructed to check the application potential of the proposed $Ni_{12}P_5/Ni/TiC$ nanocomposite capacitor electrodes. The voltage-time curve shown in Fig. 5 interprets the real working performance of this SC device. From the recorded voltage-time curve, one can see outstanding reversibility and repeatability of such a demonstrator. Namely, it features good stability. The red LED can be lighted up for about 20 s after a charging time of 10 s with a voltage decrease from 1.6 to 2.4 V. Note that, only one PC device is employed here to light up a red light-emitting diode (LED, Fig. S4†). Hence, such PCs have great potential in practical applications.

Conclusion

In summary, the $Ni_{12}P_5/Ni/TiC$ nanocomposite film synthesized on a Ti substrate features a unique structure, leading to a highly active surface and excellent conductivity. As a binder-free capacitor electrode, it exhibits high SC performance, such as a specific capacitance as high as 160.0 mF cm^{-2} at a current density of 10 mA cm^{-2}, an energy density of 42.6 W h kg^{-1} and a power density of 1550 W kg^{-1}. Such a performance results from the involvement of surface-controlled faradaic processes of the pseudoactive $Ni_{12}P_5/Ni$ species on its surface. Therefore, this $Ni_{12}P_5/Ni/TiC$ nanocomposite film is a

reliable capacitor electrode for electrochemical energy storage applications. Further activities on the structural and elemental analysis of this capacitor electrode, the effect of its structure and composition (especially the atomic variation of the elements of Ni, P, and O) on its capacitive performance, the stability improvement of this capacitor electrode, and the performance comparison of this capacitor electrode with similar electrodes in different media and under different charging/discharging conditions need to be conducted. Due to the ultrahigh energy of the as-fabricated supercapacitors, it is believed that the SCs constructed using this capacitor electrode are promising for powering multifunctional electronics, hybrid electric vehicles, and some industrial equipment in future.

Experimental

Synthesis of $Ni_{12}P_5/Ni/TiC$ nanocomposite capacitor electrodes

The synthesis steps of the $Ni_{12}P_5/Ni/TiC$ nanocomposite films are schematically illustrated in Fig. 6. In the first step, a P containing Ni_5TiO_7/TiO_2 nanocomposite film was synthesized on a Ti plate. Subsequently, impregnation and annealing treatment are applied.[15] The as-prepared Ni_5TiO_7/TiO_2 nanocomposite film is then reduced in a microwave plasma enhanced CVD (MWCVD) reactor (ASTeX A5000). The optimized conditions during the CVD process are listed as follows: a constant gas pressure of 45 Torr, a microwave power of 1400 W, a reaction time of 15 min, a hydrogen flow rate of 400 sccm and a methane flow rate of 10 sccm.

Characterization of $Ni_{12}P_5/Ni/TiC$ nanocomposite capacitor electrodes

The surface morphologies of the as-synthesized $Ni_{12}P_5/Ni/TiC$ nanocomposite films were obtained using field emission scanning electron microscopy (FESEM, Zeiss ultra55). Their superficial elemental compositions were investigated by X-ray photoelectron spectroscopy (XPS, Surface Science Instruments, SSX-100 S-probe photoelectron spectrometer, USA) using Al Kα radiation of 200 W. The XPS spectra were analyzed using the Casa XPS software. To determine the phase composition, X-ray diffraction (XRD, Philips X'Pert) measurements were performed in the 2θ range of 20–80° with a step size of 0.05° using Cu Kα radiation (40 kV, 40 mA).

Electrochemical measurements

All electrochemical measurements were conducted on a CHI660E electrochemical workstation (Shanghai Chenhua Inc., China) with a standard three-electrode cell. An Ag/AgCl (saturated 3 M KCl) electrode and a Pt wire were used as the reference electrode and the counter electrode, respectively. Cyclic voltammograms (CV) and galvanostatic charging/discharging (GCD) curves of the freshly fabricated $Ni_{12}P_5/Ni/TiC$ nanocomposite capacitor electrodes (with a geometric area of 0.05 cm^2) were recorded in 1.0 M Na_2SO_4 aqueous solutions. To estimate the energy densities and power densities of the PCs fabricated using such capacitor electrodes, a symmetrical
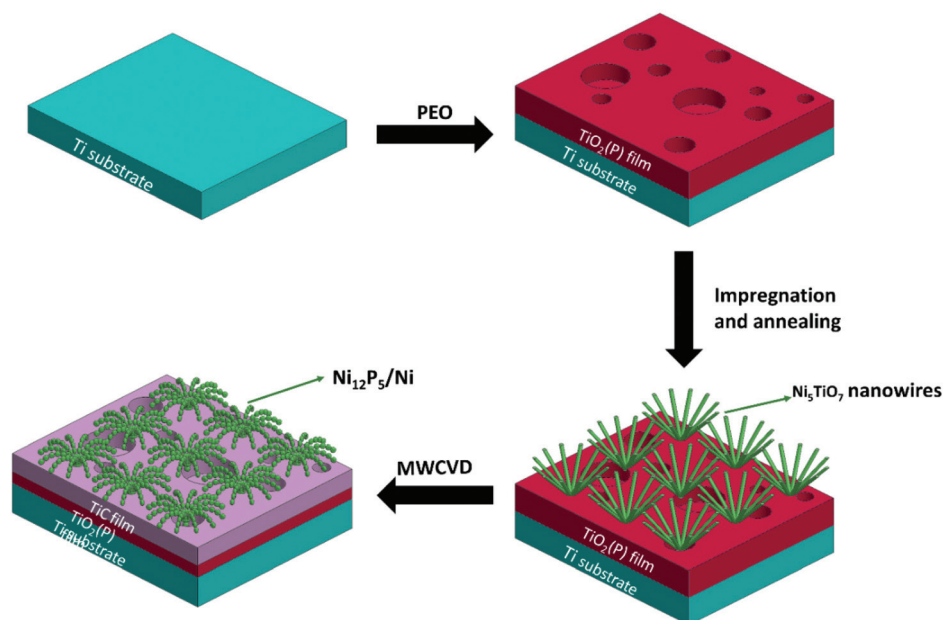
Fig. 6 Schematic illustration of the synthesis of the $Ni_{12}P_5/Ni/TiC$ composite film on a Ti substrate.

two-electrode SC device was constructed. A Nafion membrane with a thickness of 50 μm was used as the separator. Their specific capacitances (C, F cm^{-2}), energy densities (E, W h kg^{-1}), and power densities (P, W kg^{-1}) were calculated according to the reported methods.[29]

SC demonstrators

To fabricate a stand-alone SC demonstrator, two $Ni_{12}P_5/Ni/TiC$ nanocomposite capacitor electrodes were symmetrically pasted on each side of an acrylic glass cell, inside which 1 M Na_2SO_4 aqueous solution was filled. A 50 μm Nafion membrane was fixed in the middle of this cell and served as a separator. Such a SC demonstrator was then applied to light up a red LED with a working voltage of 1.6. To control the charging/discharging processes of this SC demonstrator and to record the related voltage-time curves during these charging/discharging processes, a microcontroller (Arduino UNO) was employed.[30]

Conflicts of interest

There are no conflicts to declare.

Acknowledgements

Notes and references

1 (*a*) L. L. Zhang and X. Zhao, *Chem. Soc. Rev.*, 2009, **38**, 2520–2531; (*b*) K. Zou, P. Cai, Y. Tian, J. Li, C. Liu, G. Zou, H. Hou and X. Ji, *Small Methods*, 2020, **4**, 1900763; (*c*) P. Cai, K. Zou, G. Zou, H. Hou and X. Ji, *Nanoscale*, 2020, **12**, 3677–3685; (*d*) Y. Zhu, J. Li, X. Yun, G. Zhao, P. Ge, G. Zou, Y. Liu, H. Hou and X. Ji, *Nano-Micro Lett.*, 2020, **12**, 16; (*e*) H. Hou, C. E. Banks, M. Jing, Y. Zhang and X. Ji, *Adv. Mater.*, 2015, **27**, 7861–7866.

2 D. N. Futaba, K. Hata, T. Yamada, T. Hiraoka, Y. Hayamizu, Y. Kakudate, O. Tanaike, H. Hatori, M. Yumura and S. Iijima, *Nat. Mater.*, 2006, **5**, 987–994.

3 E. C. Almeida, M. R. Baldan, J. M. Rosolen and N. G. Ferreira, *Diamond Relat. Mater.*, 2008, **17**, 1529–1533.

4 S. Yu, N. Yang, H. Zhuang, S. Mandal, O. A. Williams, B. Yang, N. Huang and X. Jiang, *J. Mater. Chem. A*, 2017, **5**, 1778–1785.

5 N. Yang, S. Yu, J. V. Macpherson, Y. Einaga, H. Zhao, G. Zhao, G. M. Swain and X. Jiang, *Chem. Soc. Rev.*, 2019, **48**, 157–204.

6 B. E. Conway, *J. Electrochem. Soc.*, 1991, **138**, 1539–1548.

7 X. Li, A. M. Elshahawy, C. Guan and J. Wang, *Small*, 2017, **13**, 1701530.

8 X. Wu, W. Xing, L. Zhang, S. Zhuo, J. Zhou, G. Wang and S. Qiao, *Powder Technol.*, 2012, **224**, 162–167.

9 K. Zhou, W. Zhou, L. Yang, J. Lu, S. Cheng, W. Mai, Z. Tang, L. Li and S. Chen, *Adv. Funct. Mater.*, 2015, **25**, 7530–7538.

10 H. Wan, L. Li, Y. Chen, J. Gong, M. Duan, C. Liu, J. Zhang and H. Wang, *Electrochim. Acta*, 2017, **229**, 380–386.

11 C. An, Y. Wang, L. Li, F. Qiu, Y. Xu, C. Xu, Y. Huang and L. J. H. Yuan, *Electrochim. Acta*, 2014, **133**, 180–187.

12 X. Li, R. Ding, L. Yi, W. Shi, Q. Xu and E. Liu, *Electrochim. Acta*, 2016, **222**, 1169–1175.

13 D. Wang, L.-B. Kong, M.-C. Liu, Y.-C. Luo and L. Kang, *Chem. – Eur. J.*, 2015, **21**, 17897–17903.

14 D. Wang, L.-B. Kong, M.-C. Liu, W.-B. Zhang, Y.-C. Luo and L. Kang, *J. Power Sources*, 2015, **274**, 1107–1113.

15 J. Xu, P. Holthaus, N. Yang, S. Jiang, A. Heupel, H. Schönherr, B. Yang, W. Krumm and X. Jiang, *Appl. Catal., B*, 2019, **249**, 155–162.

16 Y. Jiang, B. Liu, L. Yang, B. Yang, X. Liu, L. Liu, C. Weimer and X. Jiang, *Sci. Rep.*, 2015, **5**, 14330.

17 J. Xu, N. Yang, S. Heuser, S. Yu, A. Schulte, H. Schönherr and X. Jiang, *Adv. Energy Mater.*, 2019, **9**, 1803623.

18 Q. Li, J. Liang and Q. Wang, Plasma electrolytic oxidation coatings on lightweight metals, in *Book Modern surface engineering treatments*, ed. M. Aliofkhazraei, Intech, 2013.

19 Y. C. Jung, K. R. Shin, Y. G. Ko and D. H. Shin, *J. Alloys Compd.*, 2014, **586**, S548–S552.

20 Z. Huan, L. E. Fratila-Apachitei, I. Apachitei and J. Duszczyk, *J. Funct. Biomater.*, 2012, **3**, 349–360.

21 A. Yerokhin, X. Nie, A. Leyland and A. Matthews, *Surf. Coat. Technol.*, 2000, **130**, 195–206.

22 J. R. A. Sietsma, J. D. Meeldijk, J. P. den Breejen, M. Versluijs-Helder, A. J. van Dillen, P. E. de Jongh and K. P. de Jong, *Angew. Chem., Int. Ed.*, 2007, **46**, 4547–4549.

23 X. Xia, Y. Zhang, D. Chao, Q. Xiong, Z. Fan, X. Tong, J. Tu, H. Zhang and H. J. Fan, *Energy Environ. Sci.*, 2015, **8**, 1559–1568.

24 K. Chien-Sheng, T. Yao-Hsuan, L. Hong-Ying, H. Chia-Hung, S. Chih-Yen, L. Yuan-Yao, S. I. Shah and H. Chin-Pao, *Nanotechnology*, 2007, **18**, 465607.

25 Z. Huang, Z. Chen, Z. Chen, C. Lv, H. Meng and C. Zhang, *ACS Nano*, 2014, **8**, 8121–8129.

26 X. Li, A. M. Elshahawy, C. Guan and J. Wang, *Small*, 2017, **13**, 1701530.

27 X. Chen, M. Cheng, D. Chen and R. Wang, *ACS Appl. Mater. Interfaces*, 2016, **8**, 3892–3900.

28 P. Simon and Y. Gogotsi, *Nat. Mater.*, 2008, **7**, 845–854.

29 S. Yu, K. J. Sankaran, S. Korneychuk, J. Verbeeck, K. Haenen, X. Jiang and N. Yang, *Nanoscale*, 2019, **11**, 17939–17946.

30 S. Yu, N. Yang, M. Vogel, S. Mandal, O. A. Williams, S. Jiang, H. Schönherr, B. Yang and X. Jiang, *Adv. Energy Mater.*, 2018, **8**, 1702947.